

Promising high-temperature thermoelectric response of bismuth oxybromide

Deobrat Singh^{a,*}, Muhammad Sajjad^b, J. Andreas Larsson^b, Rajeev Ahuja^{a,c,*}

^a Condensed Matter Theory Group, Materials Theory Division, Department of Physics and Astronomy, Uppsala University, Box 516, 75120 Uppsala, Sweden

^b Applied Physics, Division of Materials Science, Department of Engineering Sciences and Mathematics, Luleå University of Technology, SE-97187 Luleå, Sweden

^c Applied Materials Physics, Department of Materials Science and Engineering, Royal Institute of Technology (KTH), S-10044 Stockholm, Sweden

ARTICLE INFO

Keywords:

Bismuth oxybromide
Electronic properties
Dynamical and thermal stability
Electrical and thermal transports
Figure of merit

ABSTRACT

Recently, the bismuth oxybromide quintuple-layer (QL) was experimentally realized. In the present study, we extensively examine the stability, electronic and thermal transport of bulk bismuth oxybromide (BiOBr) and QL based on first-principles calculations and the semiclassical Boltzmann transport theory. We have found that the bulk and QL BiOBr systems are dynamically and thermally stable with an indirect band gap of 2.86 and 3.08 eV, respectively. The emergence of comparatively flat bands at the top valence band favours the pronounced p-type Seebeck coefficient. Our calculated results demonstrate a high Seebeck coefficient of 1569.82 $\mu\text{V/K}$ and 1580 $\mu\text{V/K}$ for bulk and QL BiOBr materials at high temperatures. At higher temperature, the lattice thermal conductivity values of bulk are 1.32/0.23 for in-plane/out-of-plane, respectively and 1.85 W/mK in QL BiOBr, which are relatively low compared to other layered materials, e.g., MX₂ (M = Mo, W, Pt, Zr, and X = S, Se, Te). The figure of merit (ZT) turns out to be as high as 3.52 for bulk BiOBr and 1.5 for QL BiOBr at higher temperatures, suggest them as good candidates for thermoelectric applications.

Introduction

Due to the continuously increasing requirement in high-efficiency clean energy, it is necessary to develop new energy devices to resolve the energy-related problems and avoid further environmental degradation [1,2]. Thermoelectric (TE) materials can directly convert thermal energy into electrical energy; thus, they have attracted broad interest in the advancement of sustainable energy proficient technologies. Associated to other energy transformation devices, TE devices have exceptional features, including stability, noiseless, and long service life [3,4]. The TE functioning of the nanomaterials at a particular temperature is determined via the dimensionless figure of merit, defined as; $ZT = \sigma S^2 T / \kappa$, in which T, σ , κ and S represents the absolute temperature, electrical conductivity, thermal conductivity and Seebeck coefficient, respectively [5]. The thermal conductivity $\kappa = \kappa_e + \kappa_l$, in which κ_l and κ_e shows the lattice thermal conductivity and electronic thermal conductivity, respectively. The mentioned thermoelectric parameters are intensely connected and determined by the material's electronic band structure and crystal structure. The required values of ZT for the operating temperature range should be higher than 1 for thermoelectric

performance [6].

Among the currently studied materials, the family of bismuth compounds is an essential class of p-type materials for thermoelectric applications. Such as layered Bi₂Te₃ and its alloys have been studied for thermoelectric properties by Goldsmid and co-workers [7]. The Bi and Te-based materials possess "the bipolar effect" that limits the thermoelectric efficiency [8], and toxicity caused by Te, which is an element that is rare in nature. They, therefore, observe restricted use, in exacting, in large scale commercial applications. Accordingly, we explore the replacement of this family of smart materials by others built from non-toxic and earth abundant elements, which is crucial. It is exciting to note that the non-toxic bismuth oxyhalide BiOX (X = F, Cl, Br, I) are wide band gap layered materials that have outstanding photocatalytic performance and are potential candidates for optoelectronic devices [9–11]. Recently exfoliated quintuple-layer (QL) BiOBr was found to be a good candidate for photocatalytic activity [12]. Motivated by the promising properties of BiOBr, its non-toxicity and the abundance of Br compared to Te, we simulate the electronic and both thermal transport properties of bulk and QL BiOBr for TE applications. For these calculations, we use density functional theory (DFT) and the Boltzmann

* Corresponding authors at: Condensed Matter Theory Group, Materials Theory Division, Department of Physics and Astronomy, Uppsala University, Box 516, 75120 Uppsala, Sweden (D. Singh and R. Ahuja).

E-mail addresses: deobrat.singh@physics.uu.se (D. Singh), rajeev.ahuja@physics.uu.se (R. Ahuja).

<https://doi.org/10.1016/j.rinp.2020.103584>

Received 9 September 2020; Received in revised form 22 October 2020; Accepted 3 November 2020

Available online 7 November 2020

2211-3797/© 2020 The Authors. Published by Elsevier B.V. This is an open access article under the CC BY license (<http://creativecommons.org/licenses/by/4.0/>).

transport equation for phonons. The present investigation will also describe the role of quantum confinement for thermoelectric properties.

Computational details

All the calculations used the projector augmented-wave (PAW) scheme as employed in VASP package [13]. The generalized gradient approximation (GGA) in the form of Perdew-Burke-Ernzerhof (PBE) exchange-correlation potential [14] was utilized during structural relaxations, and the HSE06 hybrid functional was used for accurate electronic structure calculations. The van der Waals correction method with DFT-D2 [15] was used to correctly depict the interaction between the periodic images of the BiOBr system. The cutoff energy for plane waves was set to 650 eV. A $20 \times 20 \times 10$ ($30 \times 30 \times 15$) and $20 \times 20 \times 1$ ($30 \times 30 \times 1$) k-mesh used for self-consistent (non-self-consistent) calculations were performed for bulk and the QL systems, respectively. The Hellmann-Feynman forces dropped below 10^{-4} eV/Å was used for convergence of structural relaxation for all atoms in the present work. The electron transport properties is estimated by semi-classical Boltzmann transport equations (BTE) as employed in the BoltzTraP code [16]. In general, the relaxation time (τ) for semiconducting materials are in the order of 10^{-13} s or 10^{-14} s, [17] but no experimental value of τ is known for the studied systems. The values of τ can be deduced based on the deformation potential theory [18] but the derived values are higher than those of reality, since the theory deals mainly with carriers that are scattered from acoustic phonons. Consequently, the measured ZT values is an upper limit since from the relations, $ZT = \frac{S^2 T}{(\kappa_e/\sigma + \kappa_l/\sigma)}$ in which κ_l/σ is influenced by the τ value. Here, we opt for the room temperature $\tau = 10^{-14}$ s.

In addition, for the lattice part of thermal conductivity calculations, the Boltzmann transport equation for phonons as employed in the ShengBTE code [19] was adopted. The Phonopy code [20] with $4 \times 4 \times 2$ ($5 \times 5 \times 1$) supercell and $3 \times 3 \times 2$ ($3 \times 3 \times 1$) k-mesh for the second-order force constants were determined in bulk (QL) BiOBr, respectively. Moreover, third-order force constants were achieved via the finite displacement scheme [21] by displacing two atoms up to seven nearest

neighbors (i.e. deviation is $\approx 2.5\%$ observed when six nearest neighbor displacement is considered), consequent to an interaction range of 5.59 Å for bulk and 6.07 Å for the QL. We used a q -mesh $28 \times 28 \times 14$ and $28 \times 28 \times 1$ for bulk and QL to generate well converged lattice thermal conductivities. There is no relevant effect in our calculations by taking a very dense q -mesh $32 \times 32 \times 16$ and $32 \times 32 \times 1$. For exfoliation energy calculations using the rigorous method, explained by Jung and co-workers [22], we have used the following equations, $E_{\text{exfoliation}} = (E_{\text{mono}} - E_{\text{bulk}})/A$, in which E_{mono} , E_{bulk} are the energy of QL and bulk, respectively, and A is the surface area.

Results and discussion

Structural and electronic properties

Initially, we investigated the symmetrical structure of bulk and QL BiOBr through full structural relaxation. The atomic structure of bulk and QL BiOBr is depicted in Fig. 1 (in top and side view), and their structural parameters were computed and compared. The BiOBr structure has a simple tetragonal crystal system with space group P4/nmm, No. 64. There are 2Bi, 2O, and 2Br atoms per unite cell of a QL BiOBr. The optimized lattice parameters are found to be $a = b = 3.96$ Å, $c = 8.03$ Å in bulk BiOBr, which are consistent with the experimentally measured values of $a = b = 3.92$ Å, $c = 8.10$ Å [10]. The optimized bond lengths Br-O and Bi-Br are 2.35 Å and 3.19 Å, respectively. Moreover, QL BiOBr has a lattice parameter of 3.93 Å, and bond lengths Br-O and Bi-Br to be 2.35 Å and 3.21 Å, respectively, in consistency with previously reported work [11,23,24]. In case of QL BiOBr, the expansion of the width of its electron density compared to in bulk, where induced moments and Pauli repulsion between QLs results in shrunk width, results in the larger Bi-Br bond length, cf. graphite/graphene in ref. [25]. Furthermore, we simulated an exfoliation energy of 23.91 meV/Å², which is lower than other layered materials, such as h-BN [22] and phosphorene [22], suggesting easy mechanical exfoliation.

We have investigated the band structure and its corresponding decomposing into atomic contributions with high accuracy using the

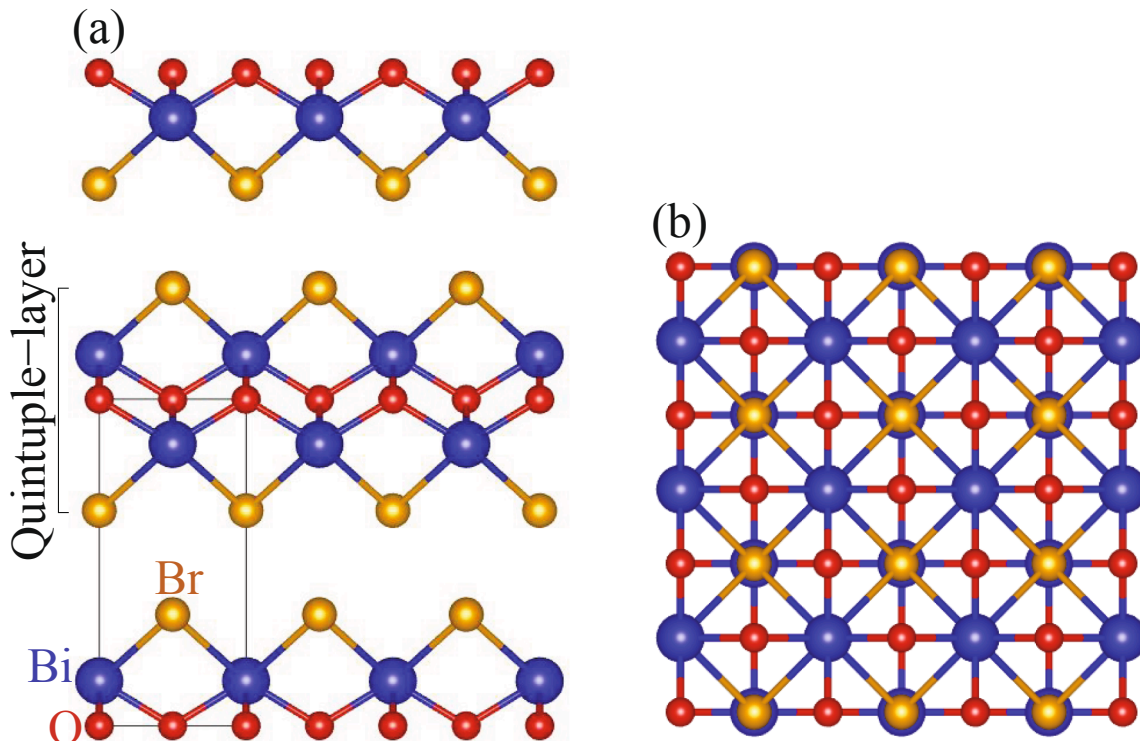


Fig. 1. (a) Side and (b) top view of geometric structure of BiOBr. The black rectangle shows the unit cell of bulk structure of BiOBr.

HSE06 hybrid functional. The band structure of bulk and QL BiOBr shows an indirect band gap, as presented in Fig. 2. The calculated band gap is found to be 2.86 eV for bulk BiOBr, which is comparable to the available experimental values (2.76 eV [9,10], 2.67 [26], 2.77–2.9 eV [11]). But it is in much better agreement than the theoretical value at PBE level (2.17 eV [26]), as expected with a hybrid functional.

Moreover, due to the quantum confinement effect, QL BiOBr has an increased band gap of 3.08 eV, which is consistent with previously reported work [23]. Also, the band gap widens for the both systems without including the spin–orbit coupling (SOC) effect (see Fig. 2). The electronic band structure of both bulk and QL BiOBr have sharp conduction band features at the Z- and Γ -point, suggesting low effective masses of electrons and a high carrier mobility. It means that there is a small amount of electronic states per eV near the conduction band minimum (CBM), which leads to a low Seebeck coefficient. Accordingly, with such band dispersion features, n-doped BiOBr exhibits excellent electrical conductivity and has a low Seebeck coefficient (S). For semi-conducting materials, the S strongly depends on the available electronic states near the Fermi-level [27]. Therefore, a large S interprets to a large

effective mass because it is directly proportional to the effective mass and the carrier mobility (μ) are inversely proportional to the effective mass ($\alpha \propto m^*$ and $\mu \propto 1/m^*$). This means that flat electronic bands/large density of states (DOS) near to the Fermi-level enhanced the S value [28,29].

From Fig. 2 (1st row), we can see that the valence band maxima are quite flat as compared to the minima of the conduction band. Therefore, these electronic bands reveal a large effective mass of holes. Besides, these electronic states near the Fermi-level in the valence band (VB) are highly degenerated (leading to large DOS), which suggest a large S and a low electrical conductivity of p-doped BiOBr. Furthermore, the atomic decomposition of the electronic band structures into Bi, O, and Br contributions is presented in 2nd, 3rd, and 4th rows in Fig. 2, respectively. The conduction band edge mainly has contributions from the Bi atoms in bulk as well as QL BiOBr. While the valence band edge is dominated by Br contributions, with smaller contributions from O and Bi atoms, as presented in Fig. 2. The electronic bands in QL BiOBr is flatter compared to bulk BiOBr. It is interesting to note that within the BiOBr QLs the electron conduction proceeds mostly through the two central Bi sub-layers, while hole conduction is close to the Br surface sub-layers.

Phonon transport properties

We have computed full phonon dispersions to verify the dynamical stability of bulk and QL BiOBr, as displayed in Fig. 3 (1st column). From Fig. 3, it can be seen that there is no imaginary frequency in the phonon dispersion profile, which indicates dynamic stability of bulk and QL BiOBr. It is evident that heavy Bi and Br atoms mainly contribute to acoustic phonons whereas light O atoms dominate the optical branch. Due to the significant differences in atomic masses, leads to a phonon gap between 5 and 7 THz. Such type of phonon characteristics leads to low lattice thermal conductivity [30]. Moreover, in the case of QL BiOBr there are three acoustical branches in which two linear dispersion profiles, i.e. a transverse acoustic (TA), a longitudinal acoustic (LA) branch, and the out-of-plane ZA branch displayed parabolic dispersion near the Γ -point. Such dispersion profile is reliable with the characteristics of phonons in monolayer nanomaterials. Additionally, we confirmed the thermal stability of bulk and QL BiOBr by ab-initio MD calculations at 900 K, which show free energy oscillates within a limited energy interval after a time of 8 ps presented in Fig. 3, lower panel. These investigations

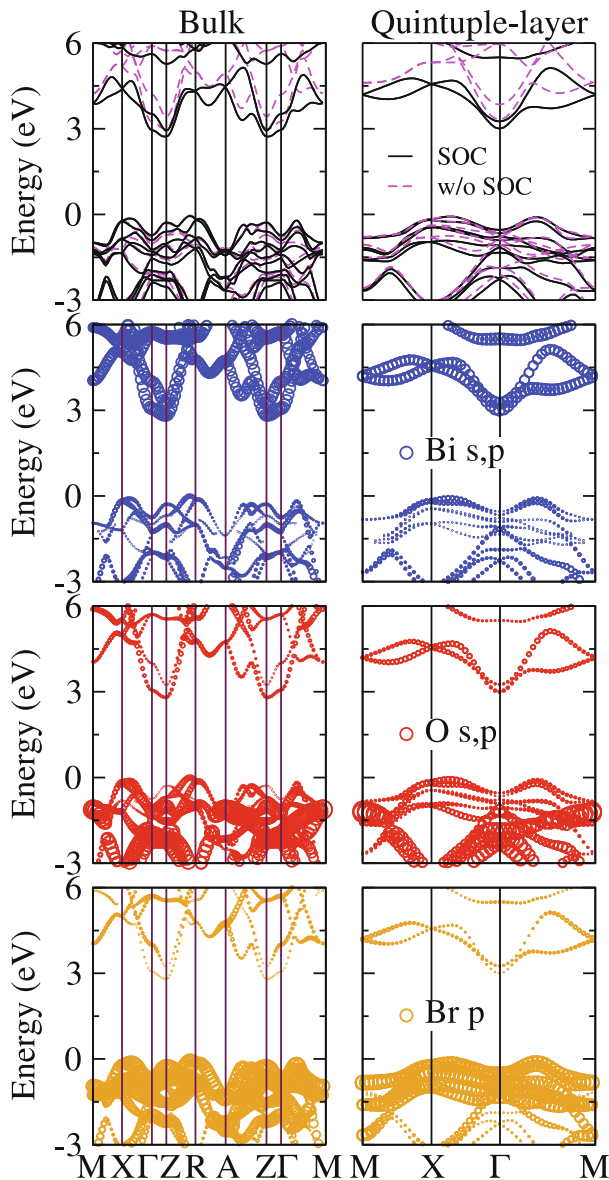


Fig. 2. Band structure and decomposed electronic band structures of bulk (1st column) and QL BiOBr (2nd column) calculated with the HSE06 hybrid-functional. The zero on y-axis displays the Fermi-level.

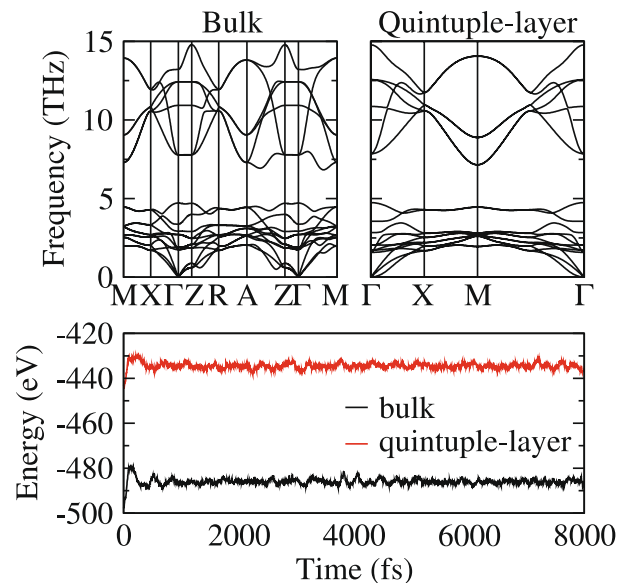


Fig. 3. The upper panel displays the phonon dispersion profile and the lower panel comprises the variation of system energy in ab-initio MD simulations at 900 K.

suggest that the bulk and QL BiOBr can maintain at as high temperatures as 900 K.

Generally, the phonon density of states offers a qualitative explanation for the role of chemical bonding on heat transport of bulk and QL BiOBr. We notice that it is the strong hybridization between Bi and Br atoms with oxidation number + 3 and −1, that gives rise to the low-frequency region (acoustical branch) below 4 THz. Since the low frequency modes are mostly reliable for heat conduction, we determine that the formation of covalent bonding between Bi and Br atoms shows a crucial role in lattice thermal transport of bulk and QL BiOBr and are reliable for the low lattice thermal conductivity.

The calculated κ_l as a function of temperature along in-plane (\parallel) and out-of-plane (\perp) directions are presented in Fig. 4 (1st column) for bulk and QL BiOBr at the temperature of 300 K, 600 K and 900 K. The points of simulated thermal conductivity fits well with the inverse temperature $\kappa_l \propto 1/T$ relationship, which is effective for the anharmonic phonon–phonon interactions [31]. The values of κ_l for bulk BiOBr are 3.98 W/mK (in-plane) and 0.70 W/mK (out-of-plane), respectively, at 300 K. The relatively very low κ_l values in the direction of out-of-plane are due to the suppressed lattice vibrations in the weak vdW bonded direction between QLs. Additionally, the lattice thermal conductivity of QL BiOBr is 5.54 W/mK at room temperature, and it also rapidly decreases with increasing temperature. At 900 K, κ_l value reaches 1.85 W/mK. The QL BiOBr has slightly larger κ_l values compared to in bulk, as seen in Fig. 4. These values are smaller in magnitude than those obtained for the transition metal dichalcogenide (TMD) monolayers such as MoS₂ (140 W/mK) [32], WS₂ (42 W/mK) [32], TiS₂ (10 W/mK) [32], ZrS₂ (11.1 W/mK) [33] HfS₂ (17 W/mK) [34]. The calculated cumulative κ_{cl} varies with the mean free path (MFP, Λ) is presented in Fig. 4 (lower panel), which shows the effect of boundary scattering in the nanostructure.

The cumulative κ_{cl} shows the dependence of the thermal conductivity of the network κ_l the sample size, and κ_l reaches its saturation value when the sample size is equal to or greater than the maximum

phonon MFPs, Λ_{\max} . The cumulative κ_{cl} also provides information about what phonon (long/short mean free path) contributes more to the thermal conductivity of the network. The analysis shows how these thermal conductivity properties may decrease with nanostructuring of the network. The QL BiOBr has a value of 407.31 nm. The simulated values of the phonon MFPs, Λ_{\max} is large. This means that nanostructuring can effectively adjust the thermal conductivity of the network [35]. To calculate another essential factor when it comes to designing with regard to nanostructuring, known as representative phonon MFP, Λ_0 we use the following relation [19];

$$k_l(\Lambda \leq \Lambda_{\max}) = \frac{k_{\max}}{1 + \Lambda_0/\Lambda},$$

where k_{\max} represents the maximal lattice thermal conductivity. From this, the values of Λ_0 for QL BiOBr is 57.98 nm.

Electrical transport properties

For the thermoelectric (TE) performance, we have calculated the σ/τ , S , κ_e/τ and ZT with respect to chemical potential (μ) as different temperature 300 K, 600 K and 900 K of bulk and QL BiOBr as shown in Fig. 5. The electrical transport properties are investigated by solving semi-classic BTE with a CRTA [16]. Now, further we replicate the effects of doping electron transport by exploiting the approximation of rigid band. Using this method, it is assumed that the nature of the band structure is invariant under light doping and the Fermi-level only moves up or down for n-type and p-type doping, respectively [36,37]. The negative and positive values of the chemical potential are associated with p- and n-type doping, respectively. The variation of S for p-type/n-type carriers are symmetric on both sides. The value of S for p-type carriers in bulk and QL BiOBr at 300 K is larger than the n-type carriers. The calculated S of 1.569 mV/K and 1.581 mV/K for bulk and QL BiOBr system. This significant improvement can be attributed to the quantum confinement effect of inducing sharp/flat states of band structure near to the Fermi [38]. When the temperature increases, the values of S slightly decrease since S is inversely proportional to absolute temperature T (see Fig. 5b). For bulk and QL BiOBr system, the μ value at which the S becomes larger is quite close to the point of charge neutrality (CNP), its magnitude displayed first increases and then decreases, and at higher temperature its value's almost same as obtained at 300 K. The variation of the electrical conductivity relaxation time scale (σ/τ) with the μ displayed in Fig. 5a changes slightly with increasing temperature. Similar to the S , electrical conductivity is less sensitive to temperature.

The electrical conductivity values we achieve are large for p-type carriers as compared to n-type carriers (see Fig. 5a). It was also seen that the electrical conductivity in in-plane direction is relatively higher than the out-of-plane direction in bulk BiOBr system while the overall electrical conductivity in its monolayer system is higher for both p- and n-types of carriers. A fairly large electrical conductivity is realized by increasing μ . The electronic states become asymmetric with respect to the Fermi-level, that is, there are different numbers of states accessible to carriers that transport both sides (p-type as well as n-type carriers) of the Fermi level, resulting in significant changes in Seebeck coefficient which also affects the electronic conductivity. At the same time, the high electronic states near the Fermi-level provides a large enough electrical conductivity. From the electronic band structures of the bulk and QL BiOBr systems we see that they have a large number of electronic states in the VB, consequentially we find a large electrical conductivity of 1.58 and 2.16 (Ωms)^{−1} for p-type carriers, respectively. In consequence, the power factor (σS^2) of bulk and QL BiOBr system will be higher for p-type carriers. Furthermore, we report the electronic thermal conductivity of the bulk and QL BiOBr system as shown in Fig. 5c. The electrical conductivity is associated with electrical thermal conductivity (κ_e) concluded as can be seen from the essential relationship known as the Wiedemann-Franz law, $\kappa_e = \sigma LT$, in which L represents the Lorenz

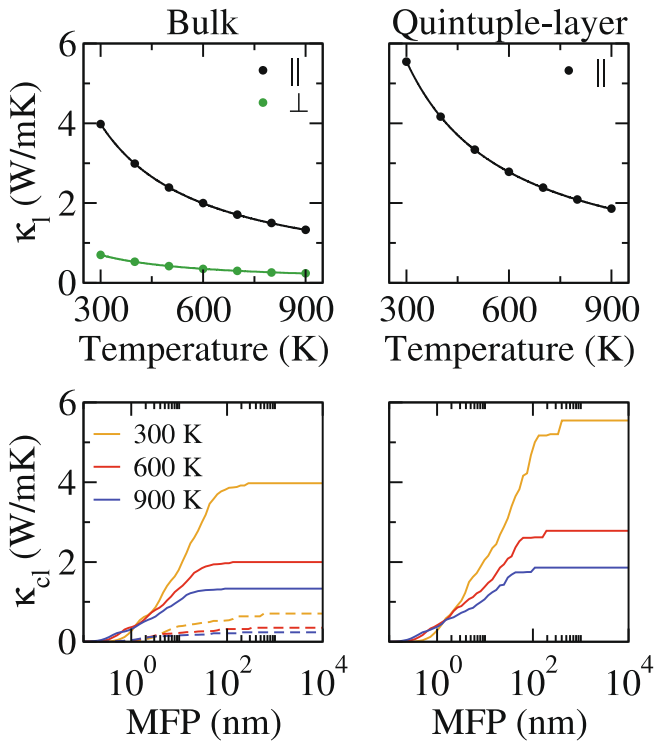


Fig. 4. Lattice thermal conductivity (1st row) and cumulative lattice thermal conductivity (2nd row) as a function of temperature and MFP, respectively. Solid curves in 1st row are the fitted values whereas the dash curves in 2nd row are the out-of-plane values.

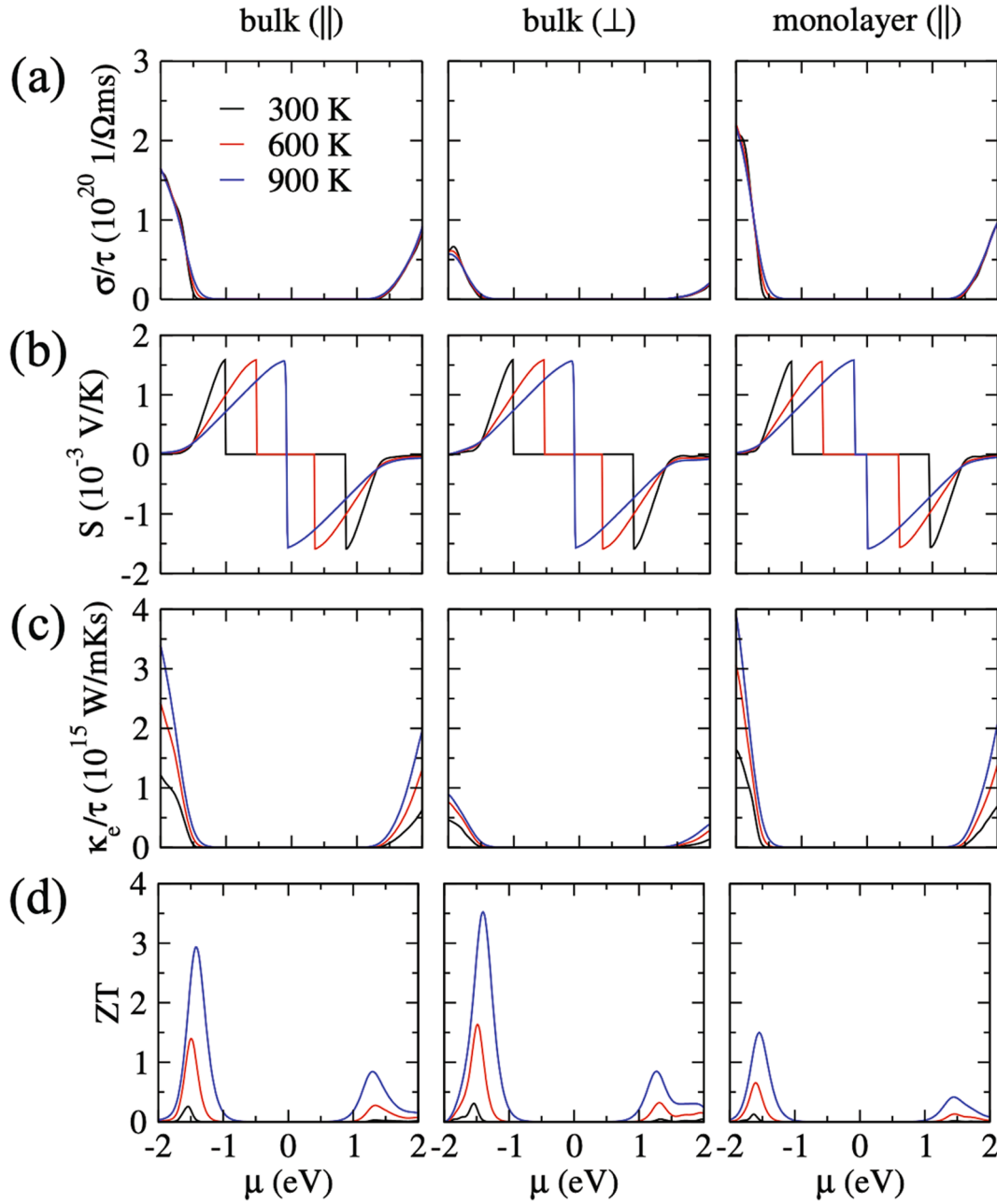


Fig. 5. Thermoelectric parameters as a function of μ at various temperature for in-plane (left panel), out-of-plane (middle panel) in bulk BiOBr and right panel in QL BiOBr: (a) Electronic conductivity (σ/τ), (b) Seebeck coefficient (S), (c) electrical thermal conductivity (κ_e/τ) and (d) figure of merit (ZT).

number [39]. Accordingly, the electrical thermal conductivity follows similar trends as the electronic conductivity (see Fig. 5).

It is well known that the TE performance of materials strongly depends on the dimensionless figure of merit (ZT). A large value of the thermoelectric figure of merit in a material indicates it would be an efficient thermoelectric material for TE applications. The Fig. 5 shows the variation of ZT as a function of the chemical potential of the BiOBr system in bulk and QL at different temperatures. Two different peaks appear for each case and each temperature. The peaks in the negative ($\mu < 0$) and positive ($\mu > 0$) chemical potentials correspond to ZT values for p- and n-type carriers, respectively. The gap between the two peaks is identical to the energy gap for the respective material and in this gap, the ZT value is zero. From the thermoelectric ZT , we can deduce that the p-type carriers have higher values as compared to for n-type carriers. The maxima ZT values for p-type carriers in bulk BiOBr for in-plane/out-of-plane are ≈ 3 and 3.5, respectively while ZT value of ≈ 1.5 in

monolayer BiOBr system at higher temperature 900 K. According to Yu et al. [40], the value of ZT was found to be 1.84 in monolayer BiOBr system. It means that the bulk form of BiOBr is a better candidate for thermoelectric applications. But the thermoelectric ZT value is higher in QL BiOBr than most of the currently considered 2D materials [38,41–46].

Conclusions

We have explored the electron and phonon transports of bulk and QL BiOBr using the DFT and the BTE approach. We have calculated the atomic decomposition of the electronic band structure and find Bi-dominated sharp features in the conduction band edge, in accordance with low effective electron mass and high electron mobility, but relatively low electronic states. The Br-dominated valence band edge has flat features and degenerate states and, hence, leading to high effective hole

mass and large DOS contribution. The band structure suggests a low/high Seebeck coefficient for n-type/p-type carriers in BiOBr. Our results displayed a high Seebeck coefficient of 1569.82 $\mu\text{V/K}$ and 1580 $\mu\text{V/K}$ for bulk and QL BiOBr system at high temperature. The phonon dispersion profile displays dynamic stability with strong optical and acoustic phonon coupling. Contribution of every vibrational branch to the lattice thermal conductivity was simulated, and the size dependency of the lattice thermal conductivity was also examined. A relatively low lattice thermal conductivity (i.e. 1.32/0.23 for in-plane/out-of-plane in bulk and 1.85 W/mK in QL BiOBr) compared to other layered systems was observed and suggests QL BiOBr to be a favorable material for thermoelectric applications. The larger phonon mean free paths for the QL result in the sizeable in-plane lattice thermal conductivities that can effectively be reduced by nanostructuring. Additionally, the values of ZT in bulk BiOBr are more than 3.52 while it QL has 1.5 at higher temperature. These investigations suggest that the bulk form of BiOBr system is a good candidate for thermoelectric devices.

Data availability statement

The raw/processed data required to reproduce these findings cannot be shared at this time due to legal or ethical reasons. Data are however available from the authors upon reasonable request.

CRediT authorship contribution statement

Deobrat Singh: Investigation, Methodology, Visualization, Writing - original draft, Writing - review & editing. **Muhammad Sajjad:** Conceptualization, Formal analysis, Investigation, Methodology, Writing - review & editing, Validation. **J. Andreas Larsson:** Funding acquisition, Resources, Software, Writing - review & editing, Validation. **Rajeev Ahuja:** Funding acquisition, Project administration, Resources, Software, Supervision, Writing - review & editing, Validation.

Declaration of Competing Interest

The authors declare that they have no known competing financial interests or personal relationships that could have appeared to influence the work reported in this paper.

Acknowledgments

D.S. and R.A. thanks Olle Engkvists stiftelse (198-0390), Carl Tryggers Stiftelse for Vetenskaplig Forskning (CTS: 18:4) and Swedish Research Council (VR-2016-06014) for financial support. JAL would like to thank VR, Knut and Alice Wallenberg Foundation, Kempe Foundations, Länsstyrelsen Norrbotten and Interreg Nord for financial support. SNIC and SNAC are acknowledged for providing the computing facilities, through HPC2N, NSC and PDC.

References

- [1] Zhu T, Liu Y, Fu C, Heremans JP, Snyder JG, Zhao X. Compromise and synergy in high-efficiency thermoelectric materials. *Adv Mater* 2017;29(14):1605884. <https://doi.org/10.1002/adma.291410.1002/adma.201605884>.
- [2] Chen Z-G, Han G, Yang L, Cheng L, Zou J. Nanostructured thermoelectric materials: current research and future challenge. *Progr Nat Sci Mater Int* 2012;22(6):535–49.
- [3] Ortega S, Ibáñez M, Liu Yu, Zhang Yu, Kovalenko MV, Cadavid D, Cabot A. Bottom-up engineering of thermoelectric nanomaterials and devices from solution-processed nanoparticle building blocks. *Chem Soc Rev* 2017;46(12):3510–28.
- [4] Ge Z-H, Zhao L-D, Wu Di, Liu X, Zhang B-P, Li J-F, He J. Low-cost, abundant binary sulfides as promising thermoelectric materials. *Mater Today* 2016;19(4):227–39.
- [5] Yang J, Yip H-L, Jen A-Y. Rational design of advanced thermoelectric materials. *Adv Energy Mater* 2013;3(5):549–65.
- [6] Goldsmid HJ, editor. *Thermoelectric refrigeration*. Boston, MA: Springer US; 1964.
- [7] Goldsmid H. Bismuth telluride and its alloys as materials for thermoelectric generation. *Materials (Basel)* 2014;7:2577–92.
- [8] Poudel B, Hao Q, Ma Y, Lan Y, Minnich A, Yu B, Yan X, Wang D, Muto A, Vashaee D, Chen X, Liu J, Dresselhaus MS, Chen G, Ren Z. High-thermoelectric performance of nanostructured bismuth antimony telluride bulk alloys. *Science* 2008;320(5876):634–8.
- [9] Ling-Li W, Wan-Hong Ma, Shu-Lian W, Yu Z, Man-Ke J, Rui-Ping Li, Ai-Qing Z, Ying-Ping H. The contrastive research in the photocatalytic activity of BiOBr synthesized by different reactants. *J Nanomater* 2012;2012:1–9.
- [10] An H, Du Y, Wang T, Wang C, Hao W, Zhang J. Photocatalytic properties of BiOX (X = Cl, Br, and I). *Rare Met* 2008;27(3):243–50.
- [11] Paudel S, Adhikari PR, Upadhyay OP, Kaphle GC, Srivastava A. First Principles Study of Electronic and Optical Properties of Pristine and X (Cu, Ag And Au) Doped BiOBr. *J Inst Sci Technol* 2018;22:63–9.
- [12] Wu Ju, Li X, Shi W, Ling P, Sun Y, Jiao X, Gao S, Liang L, Xu J, Yan W, Wang C, Xie Yi. Efficient visible-light-driven CO₂ reduction mediated by defect-engineered BiOBr atomic layers. *Angew Chem Int Ed* 2018;57(28):8719–23.
- [13] Kresse G, Furthmüller J. Efficient iterative schemes for ab initio total-energy calculations using a plane-wave basis set. *Phys Rev B* 1996;54(16):11169–86.
- [14] Perdew JP, Burke K, Ernzerhof M. Generalized gradient approximation made simple. *Phys Rev Lett* 1996;77(18):3865–8.
- [15] Grimme S. Semiempirical GGA-type density functional constructed with a long-range dispersion correction. *J Comput Chem* 2006;27(15):1787–99.
- [16] Madsen GKH, Carrete J, Verstraete MJ. BoltzTraP2, a program for interpolating band structures and calculating semi-classical transport coefficients. *Comput Phys Commun* 2018;231:140–5.
- [17] Brennan KF. *The physics of semiconductors*. Cambridge University Press; 1999.
- [18] Bardeen J, Shockley W. Deformation potentials and mobilities in non-polar crystals. *Phys Rev* 1950;80(1):72–80.
- [19] Li Wu, Carrete J, Katcho NA, Mingo N. ShengBTE: a solver of the Boltzmann transport equation for phonons. *Comput Phys Commun* 2014;185(6):1747–58.
- [20] Togo A, Tanaka I. First principles phonon calculations in materials science. *Scr Mater* 2015;108:1–5.
- [21] Esfarjani K, Stokes HT. Method to extract anharmonic force constants from first principles calculations. *Phys Rev B* 2008;77(14). <https://doi.org/10.1103/PhysRevB.77.144112>.
- [22] Jung JH, Park C-H, Ihm J. A rigorous method of calculating exfoliation energies from first principles. *Nano Lett* 2018;18(5):2759–65.
- [23] Zhang X, Li B, Wang J, Yuan Yu, Zhang Q, Gao Z, Liu L-M, Chen L. The stabilities and electronic structures of single-layer bismuth oxyhalides for photocatalytic water splitting. *PCCP* 2014;16(47):25854–61.
- [24] Zhou S, Shi T, Chen Z, Kilin D, Shui L, Jin M, et al. First-Principles Study of Optoelectronic Properties of the Noble Metal (Ag and Pd) Doped BiOX (X = F, Cl, Br, and I) Photocatalytic System. *Catalysts* 2019;9:198.
- [25] Koumpouras K, Larsson JA. Distinguishing between chemical bonding and physical binding using electron localization function (ELF). *J Phys: Condens Matter* 2020;32(31):315502. <https://doi.org/10.1088/1361-648X/ab7fd8>.
- [26] Huang H, Han Xu, Li X, Wang S, Chu PK, Zhang Y. Fabrication of multiple heterojunctions with tunable visible-light-active photocatalytic reactivity in BiOBr–BiOI full-range composites based on microstructure modulation and band structures. *ACS Appl Mater Interfaces* 2015;7(1):482–92.
- [27] He J, Tritt TM. Advances in thermoelectric materials research: looking back and moving forward. *Science* 2017;357(6358):eaak9997. <https://doi.org/10.1126/science.aak9997>.
- [28] Maignan A, Caignaut V, Raveau B, Khomskii D, Sawatzky G. Thermoelectric power of HoBaCo. *Phys Rev Lett* 2004;93:026401.
- [29] Lewis FB, Saunders NH. The thermal conductivity of NiO and CoO at the Neel temperature. *J Phys C: Solid State Phys* 1973;6(15):2525–32.
- [30] Sajjad M, Singh N, Sattar S, De Wolf S, Schwingschlögl U. Ultralow lattice thermal conductivity and thermoelectric properties of monolayer Ti₂O. *ACS Appl Energy Mater* 2019;2(5):3004–8.
- [31] Ziman JM. *Electrons and phonons*. Oxford University Press; 2001.
- [32] Naghavi SS, He J, Xia Yi, Wolverton C. Pd₂Se₃ monolayer: a promising two-dimensional thermoelectric material with ultralow lattice thermal conductivity and high power factor. *Chem Mater* 2018;30(16):5639–47.
- [33] Ding G, Chen J, Yao K, Gao G. Convergence of separate orbitals for enhanced thermoelectric performance of layered ZrS₂. *New J Phys* 2017;19:073036.
- [34] Gu X, Yang R. Phonon transport in single-layer transition metal dichalcogenides: a first-principles study. *Appl Phys Lett* 2014;105(13):131903. <https://doi.org/10.1063/1.4896685>.
- [35] Balandin A, Wang KL. Significant decrease of the lattice thermal conductivity due to phonon confinement in a free-standing semiconductor quantum well. *Phys Rev B* 1998;58(3):1544–9.
- [36] Parker D, Singh DJ. Potential thermoelectric performance from optimization of hole-doped Bi₂Se₃. *Phys Rev X* 2011;1:021005.
- [37] Singh DJ. Electronic and thermoelectric properties of CuCoO₂: density functional calculations. *Phys Rev B* 2007;76:085110.
- [38] Wang FQ, Zhang S, Yu J, Wang Q. Thermoelectric properties of single-layered SnSe sheet. *Nanoscale* 2015;7(38):15962–70.
- [39] Tritt TM. Thermoelectric phenomena, materials, and applications. *Annu Rev Mater Res* 2011;41(1):433–48.
- [40] Yu J, Li T, Sun Q. Single-layer BiOBr: an effective p-type 2D thermoelectric material. *J Appl Phys* 2019;125(20):205111. <https://doi.org/10.1063/1.5098826>.
- [41] Medrano Sandomas L, Teich D, Gutierrez R, Lorenz T, Pecchia A, Seifert G, Cuniberti G. Anisotropic thermoelectric response in two-dimensional puckered structures. *J Phys Chem C* 2016;120(33):18841–9.
- [42] Zhu X-L, Liu P-F, Xie G, Zhou W-X, Wang B-T, Zhang G. Thermoelectric Properties of Hexagonal M₂C₃ (M = As, Sb, and Bi) Monolayers from First-Principles Calculations. *Nanomaterials* 2019;9:597.

- [43] Ding G, Gao G, Yao K. High-efficient thermoelectric materials: the case of orthorhombic IV-VI compounds. *Sci Rep* 2015;5(1). <https://doi.org/10.1038/srep09567>.
- [44] Wang Q, Han L, Wu L, Zhang T, Li S, Lu P. Strain effect on thermoelectric performance of InSe monolayer. *Nanoscale Res Lett* 2019;14(1). <https://doi.org/10.1186/s11671-019-3113-9>.
- [45] Mishra P, Singh D, Sonvane Y, Ahuja R. Two-dimensional boron monochalcogenide monolayer for thermoelectric material. *Sustainable Energy Fuels* 2020;4(5): 2363–9.
- [46] Singh D, Kansara S, Gupta SK, Sonvane Y. Single layer of carbon phosphide as an efficient material for optoelectronic devices. *J Mater Sci* 2018;53(11):8314–27.